Improving Chandra High Resolution Camera event positions via corrections to crossed-grid charge detector signals

M. Juda, G. K. Austin, J. H. Chappell, J. J. Gomes, A. T. Kenter, R. P. Kraft, S. S. Murray, and M. V. Zombeck

Harvard-Smithsonian Center for Astrophysics,
60 Garden St, Cambridge, MA 02138

ABSTRACT

The High Resolution Camera (HRC) on-board the Chandra X-ray Observatory (CXO) provides the highest resolution X-ray images of celestial sources ever taken. Unfortunately, ringing in the electronics compromises the position readout signals for some of the events. The compromised signals affect the angular resolution that can be achieved. We present an empirically derived algorithm that can be used in ground processing of the data to minimize the impact of the ringing on the calculated event positions.

Keywords: X-ray detectors, microchannel plates, crossed-grid charge detector, High Resolution Camera, Chandra X-ray Observatory

1. INTRODUCTION

The Chandra X-ray Observatory (CXO), the third in NASA's "Great Observatories" series, is designed for high-resolution imaging and spectroscopy in the energy range 0.07 to 10.0 keV.[1] The CXO optic, the High-Resolution Mirror Assembly (HRMA),[2] provides the highest-resolution celestial X-ray images ever achieved with a 50% encircled energy radius of $\sim$0.3 arcseconds. The CXO has two focal plane instruments: the Advanced CCD Imaging Spectrometer (ACIS)[3,4] and the High Resolution Camera (HRC).[5] High resolution spectroscopy is achieved by inserting either the High Energy Transmission Grating (HETG)[6] or Low Energy Transmission Grating (LETG)[7] into the optical path.

The HRC contains microchannel plate based X-ray detectors, similar to the High Resolution Imagers from both the *Einstein* and *ROSAT* missions. There are two detectors within the HRC: one designed for imaging, the HRC-I, and one designed to be used as the read-out for the LETG, the HRC-S. Details of the calibration and early mission on-orbit performance of the HRC detectors are given in Kenter et al. (2000)[8] and Kraft et al. (2000).[9]

Since launch there have been a few surprises in the HRC performance.[10,11] This paper describes one of those surprises, an instrumental blurring of the images. In section 2 we describe how the HRC generates the data that are used to determine X-ray event positions. Section 2 also contains a description of a hardware problem that affects the data from some of the events. In section 3 we describe the signature of the corrupted data. Section 4 contains an empirically derived correction algorithm that can be used to minimize the amount of instrumental blur and an example of the results of its application. Finally in section 5 we have some concluding remarks.

Send correspondence to M. Juda, E-mail: mjuda@cfa.harvard.edu

Copyright 2000 Society of Photo-Optical Instrumentation Engineers.
This paper was published in SPIE Proceedings 4140, 155 and is made available as an electronic reprint with permission of SPIE. One print or electronic copy may be made for personal use only. Systematic or multiple reproduction, distribution to multiple locations via electronic or other means, duplication of any material in this paper for a fee or for commercial purposes, or modification of the content of the paper are prohibited.

2. EVENT POSITION DETERMINATION

The HRC uses a crossed grid charge detection scheme to register the position of the charge cloud produced by an event emerging from the bottom of the MCP stack.[12] This method was used for the *Einstein* and *ROSAT* HRIs. A detailed explanation of the operating principle of the crossed grid charge detector (CGCD) can be found in Chappell & Murray (1989).[13] Briefly, the HRC CGCD consists of two planes of wires that run perpendicular to each other. Adjacent wires along a single axis are connected via resistors. Every eighth wire is connected to a charge amplifier; this location is known as a tap. The charge that is deposited on an individual wire is divided between the two nearest taps in inverse proportion to the ratio of resistances from the wire to the taps. Using the signals from the three amplifiers centered on the charge cloud (A_{i-1}, A_i, and A_{i+1}), the event position relative to the central amplifier (tap i) can be determined via a "three tap position algorithm"[13]:

$$f_p = \frac{A_{i+1} - A_{i-1}}{A_{i-1} + A_i + A_{i+1}}. \quad (1)$$

This algorithm can be further modified to account for "gaps" caused by incomplete charge collection.[13] This f_p is added to the event's coarse position, given by the number of the tap that is the center of the distribution, and scaled to produce an event position. The calculation of the event position is not performed on-board but rather the coarse position and the size of the three tap signals for each axis are telemetered to the ground and the calculation is done in the ground processing.

The event coarse position is determined by the HRC instrument by the following process. An event is detected when the signal from the back MCP exceeds a commandable threshold value. Once the event is detected, the signals from the taps on the CGCD are sampled and compared to a threshold. This tap-signal threshold is dynamically adjusted, based on the size of the MCP signal, in order to avoid having too many of the tap signals above threshold. A set of "UP" and "DOWN" priority encoders are used to determine the lowest and highest tap numbers for which the signals exceeded the threshold. These two numbers are averaged to return a candidate coarse position; the half-integer values are truncated. Given a candidate coarse position on tap number i, a multiplexer selects four neighboring tap signals, $i-1$, i, $i+1$, and $i+2$, for the next step in coarse position determination. The signal on the candidate coarse position tap (i) and that on the next higher numbered tap ($i+1$) are compared to determine which tap has the larger signal; that tap number becomes the selected coarse position. The coarse position tap signal and the two adjacent signals are then selected for digitization and insertion into telemetry. The three signals are input to amplifiers with selectable gains for which the gain settings are determined by the amplitude of the pulse from the bottom MCP. The selected scale factor appears in the telemetry for each event. Finally, the three signals are input to ADCs for conversion to serial digital data and buffering for output into the telemetry stream.

2.1. "The Problem"

The gains of amplifiers at the input to the ADCs were reduced late in the program in order to accommodate a larger than expected gain in the MCP output.[14] Unfortunately, the gain reduction led to a marginal instability in the amplifiers which was discovered too late to be corrected. This instability corrupts the data of the telemetered position taps under a specific set of conditions: the least sensitive amplifier scale factor is selected and the initial candidate for the coarse position is incorrect. When an even number of taps have signals that are above threshold we expect that half the time the initial candidate for the coarse position will not have the largest signal (i.e when the event position is more than half-way to the next-higher-numbered tap). In the case where the next-higher-numbered tap is the coarse position that is selected, the event will have $A_{i-1} > A_{i+1}$ in equation 1 so the event will be on the negative side of the tap. Changing the coarse position from the initial candidate to the next-higher-numbered tap causes changes in the size of the signals going into the amplifiers with selectable gains. Because of the marginal instability on the least sensitive scale, there is a ringing, generated when the signals are switched, that is still present at the time that the signals are sampled. Examples of this behavior, taken in the laboratory using flight-like electronics, are shown in figure 1. The ringing results in offsets on the telemetered tap values from their true values, with the smallest signal of the triplet for an axis being the most affected. When the event position is calculated from the corrupted data, the positions are incorrectly determined and can be off by a few pixels. It is possible to at least partially correct the data for the effects of the ringing during ground processing.

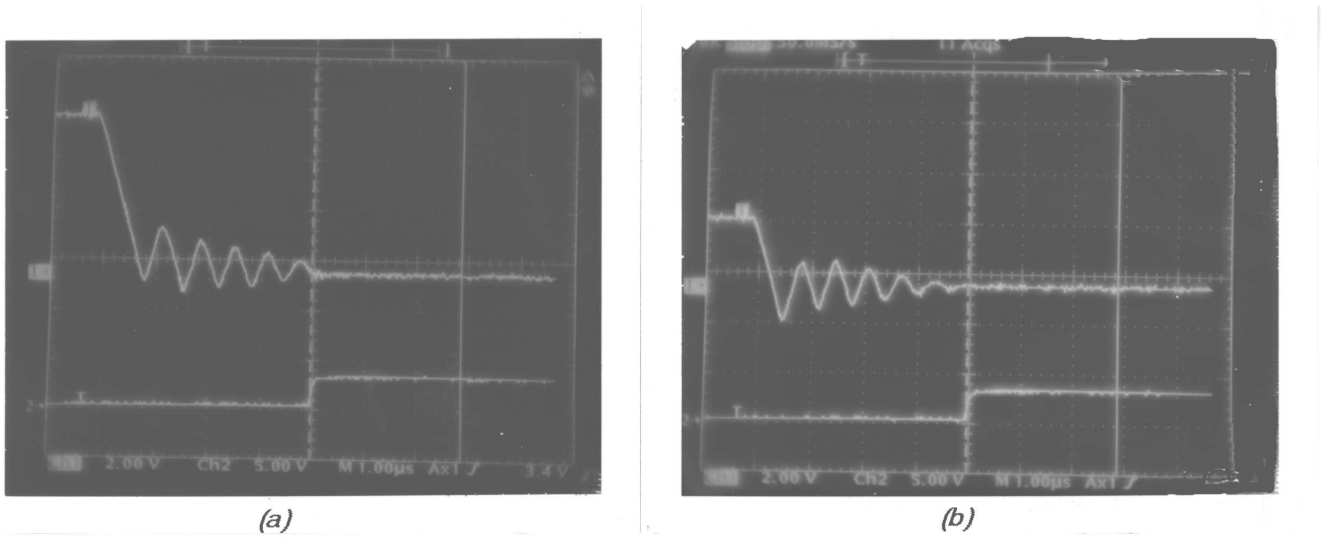

Figure 1. Examples of ringing on a tap signal, as observed in a laboratory version of the HRC flight electronics. The amplitude of the change in the signal is higher in (a) than in (b). The vertical line at the center of each photograph is the point at which the signal is sampled. The signal in (a) is sampled at an earlier phase in the oscillation than the signal in (b).

3. CHARACTERISTICS OF SIGNAL CORRUPTION

Ideally we would develop an algorithm for correcting the tap data through a detailed analysis of the voltage signals; we do not have this capability with the flight instrument. We can use the laboratory electronics to understand the general characteristics required to develop the correction algorithm but the detailed corrections will not be the same. However, we can examine the telemetered tap values in the context of the knowledge gained from the laboratory and use them to derive the detailed corrections.

Figure 2 is a scatter plot of fraction of the signal that is on the center tap versus the fine position (f_p) for a subset of the events that are not affected by the ringing from an HRC-I observation of supernova remnant Cas-A. The events lie in a well-defined band in this parameter space that has a hyperbolic shape.[10] The well-defined hyperbolic shape implies that there is a well-defined relation between the relative sizes of the tap signals as a function of position across the tap. We can use these relationships to study the deviations in the tap signals produced by the ringing in the signals. Figure 3 shows two other subsets of data from the same observation as figure 2; the key difference among the three subsets is the size of the total charge collected on the CGCD. In both of the latter two subsets, the locus of points on the positive fine position side follows the same curve as the data displayed in figure 2, while most of the events on the negative side are systematically off of the hyperbola that describes the shape of good positions. Moreover, there are differences between these two subsets in their deviations from the locus of good points which depend on the size of the signal measured on the grid. One difference between the two to note is that the fine position at which the discontinuity off of the curve occurs becomes more negative as the pulse height increases. This effect can be explained by the fact that the ringing requires there to be an even number of taps exceeding a threshold and larger signals allow the events to occur farther away from the center of the tap before the number of taps above threshold changes from three to two.

The event data plotted in figures 2 and 3 has already been somewhat processed; better insight into how the data is being corrupted can be obtained by plotting raw tap data. Figure 4 is a scatter plot of V-axis tap values from a subset of the events on the least sensitive amplifier scale. In telemetry processing, the V-axis tap signals are given the names AV1, AV2, and AV3, where AV2 is the signal from the coarse position tap, i, and AV1 and AV3 are the signals from the $i-1$ or left and $i+1$ or right taps respectively. Corresponding name assignments are given to the telemetered U-axis tap signals. The events in figure 4a are not affected by the ringing in the amplifier, while those

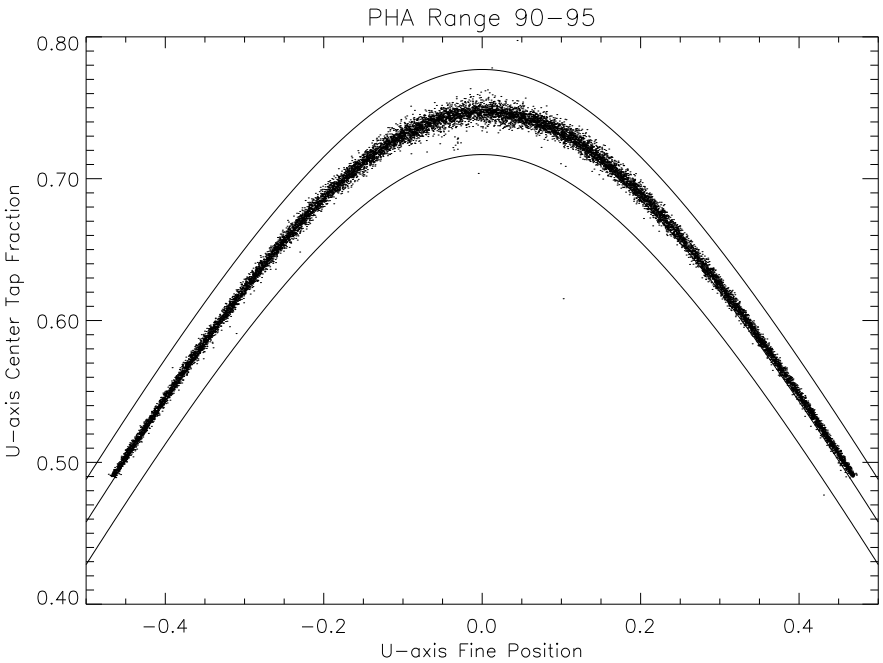

Figure 2. Plot of the fraction of the charge on the center tap versus fine position for events showing the "hyperbolic" shape of the locus of well defined positions. The solid lines are hyperbolas that define the mean locus of good event positions and limits that are used for screening test used to preferentially select X-ray events relative to background events or events that otherwise have poorly determined positions.

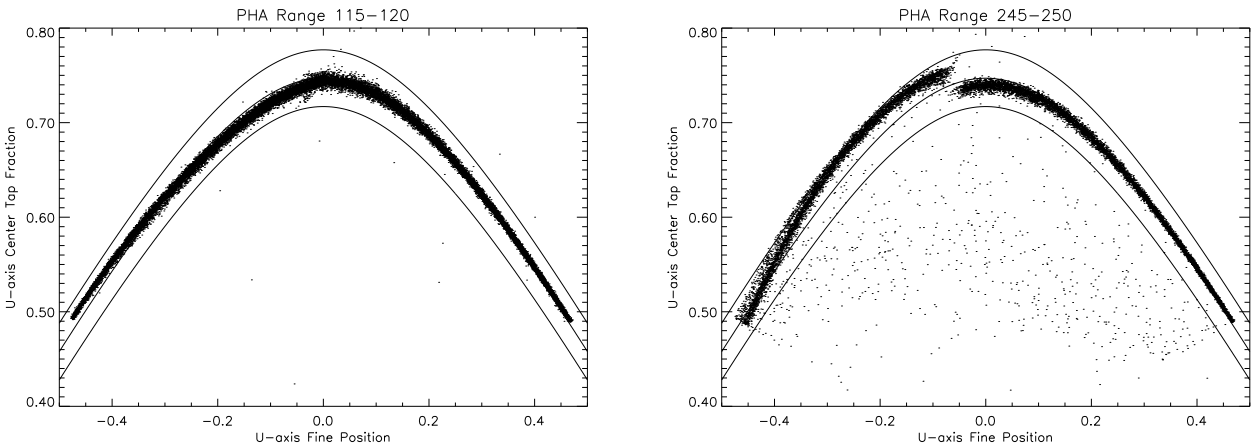

(a) (b)

Figure 3. Plot of the fraction of the charge on the center tap versus fine position for events showing the effect of ringing on the fine positions. In (a) the subset is selected from the lower end of the pulse height range affected by the ringing. In (b) the subset is selected from the upper end of the pulse height range affected by the ringing.

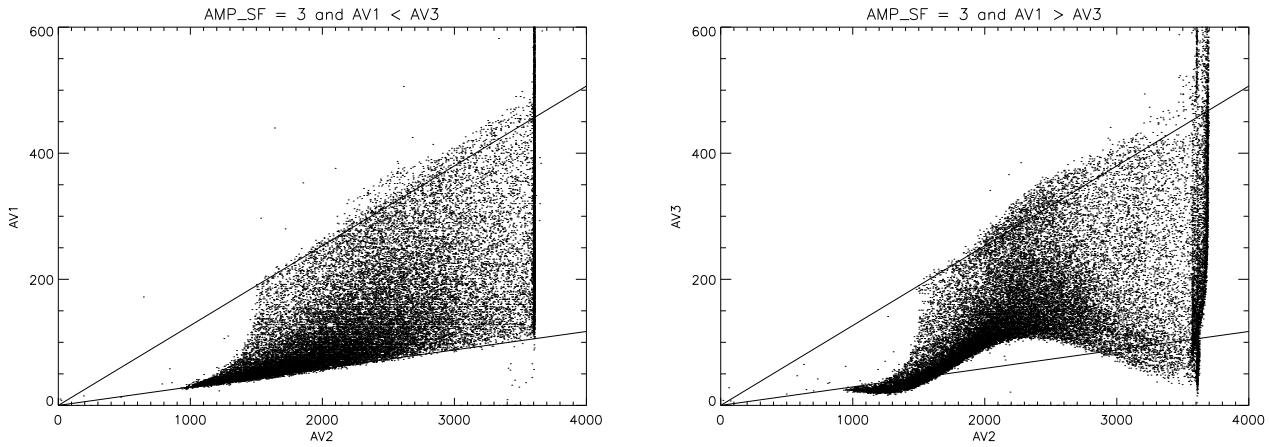

(a) (b)

Figure 4. V-axis tap values: a) Left tap (AV1) vs center tap (AV2) for events that occur to the right of the center tap. b) Right (AV3) tap vs center tap (AV2) for events that occur to the left of the center tap. The solid lines from the origin show the expected linear relationship between the tap values at the center and edge of the tap as the signals increase in amplitude. A sinusoidal pattern caused by the amplifier ringing is clearly evident in panel b.

in figure 4b are. The corruption of the right side tap data for events occurring on the left (negative) side of the tap can be seen as the sinusoidal pattern relative the expected linear relationship with increasing amplitude.

It is not initially obvious why a damped ringing of the amplifier signals should introduce a sinusoidal distortion. If the sampling occurs at a fixed time after the tap selection is switched, we would naively expect the size of the error to depend only on the amplitude difference between the signals; the period and decay-time constants should be fixed by resistances and capacitances in the electrical circuit. An examination of the data in figure 1 reveals that the ringing is initially limited by the slew rate in the amplifier. The slew-rate limitation introduces an amplitude dependent shift in the phase of the oscillation at the time of sampling.

3.1. Sinusoidal Deviations

A better look at the sinusoidal distortion of the right tap signal can be obtained by restricting the range of values of the left tap relative to the central tap; this effectively restricts the events to a limited range of fine positions. With this selection of events it is also possible to remove the expected linear trend between the two tap values and observe the sinusoidal distortion directly. Figure 5 shows the AV3 deviations from the expected value for only those events for which AV1/AV2 is in the range 0.98-1.00; these are the events near the negative edge of the tap ($f_p \simeq -0.5$). The amplitude of the sinusoidal distortion increases as the size of the center tap signal increases. From the spacing between the sinusoid zero crossings, it is also apparent that the period of the sinusoid increases with increasing center tap signal. We can empirically characterize the distortion with a sinusoid in which the amplitude and period are linear functions of the center tap value:

$$\Delta\mathrm{AV3} = \left(\frac{\mathrm{AV2}+b}{a}\right)\sin\left(2\pi\frac{\mathrm{AV2}-\phi}{c\mathrm{AV2}+d}\right). \tag{2}$$

The period function can be determined from the "zero crossing" points of the deviations from the expected value. There is a multiplicity in period solutions depending on the phase adopted for the zero-crossing points (i.e. does the crossing at AV2 $\approx$ 1640 correspond to 0.5, 1.0, 1.5,... cycles). Once the period function is selected, the amplitude function can be determined from the observed deviations at selected AV2 values, correcting for the magnitude of the sine function.

Figure 6 shows a plot similar to figure 5 but for events with AV1/AV2 in the range 0.295-0.305. In this figure the sinusoid that is plotted with a dashed line is the same as the one in figure 5; clearly, the zero-crossing points have

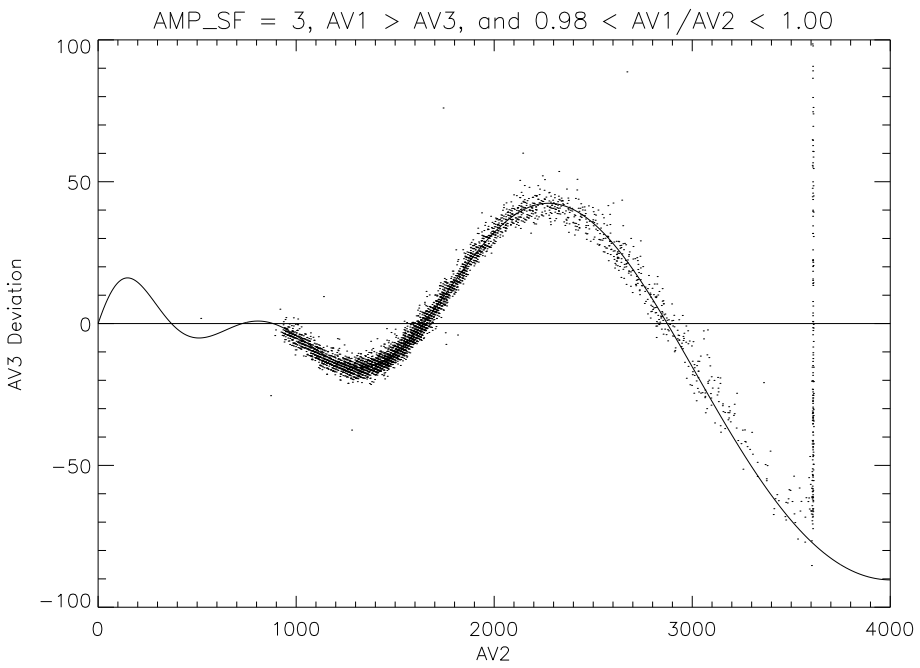

Figure 5. Deviations of the corrupted AV3 tap signals from their expected values. The events are selected to be from $f_p \simeq -0.5$ by having AV1 $\approx$ AV2. The solid curve is an empirically derived sinusoid model for the distortion.

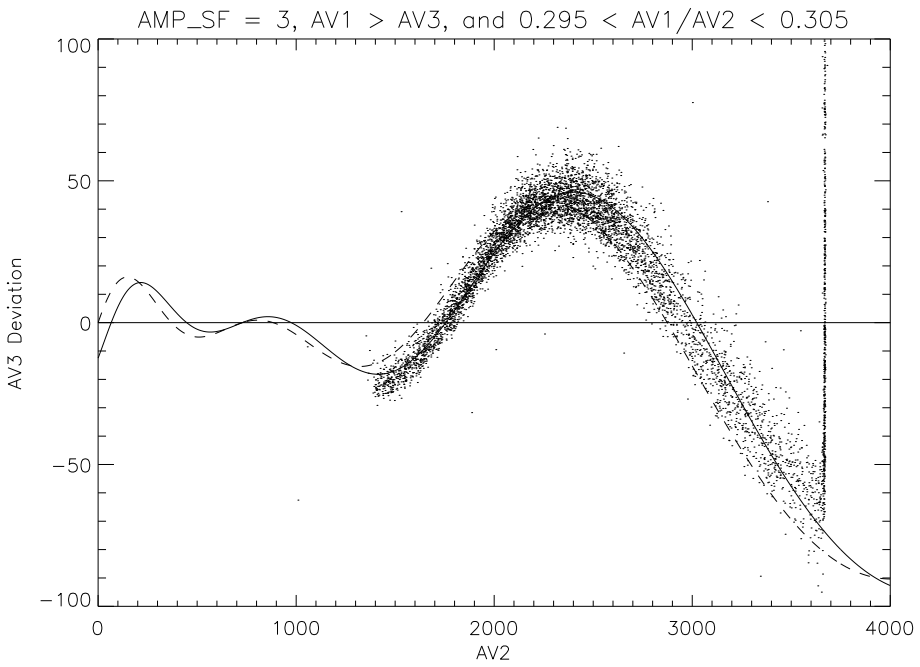

Figure 6. Deviations of the corrupted AV3 tap signals from their expected values. The events are selected to have AV1/AV2 in the range 0.295-0.305. The dashed curve is the same sinusoid as plotted in figure 5. The solid curve differs from the dashed curve only in the value of ϕ used in the sinusoid described in equation 2.

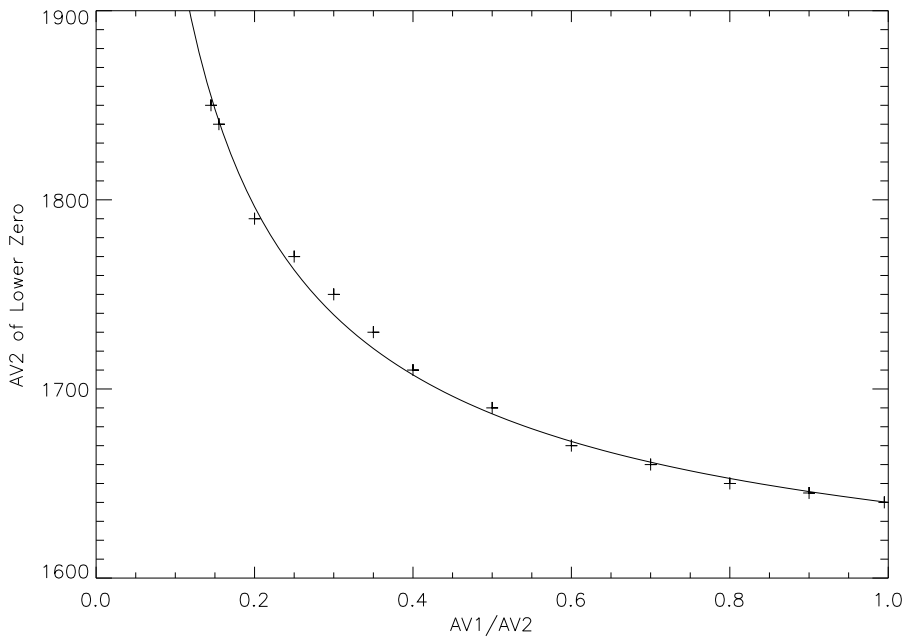

Figure 7. V-axis sinusoidal deviation lower zero-crossing point as a function of AV1/AV2.

shifted. The sinusoid plotted with a solid line differs from the one plotted with a dashed line only by the value of ϕ in equation 2. Since the zero-crossing points shift as AV1/AV2 changes, the sinusoid should be modified by making ϕ a function of AV1/AV2, ϕ(AV1/AV2). Figure 7 is a plot of the lower of the two zero-crossing points as a function of AV1/AV2. The solid curve is a function of the form:

$$\alpha + \beta \left(\left(\frac{\mathrm{AV2}}{\mathrm{AV1}} \right)^{\gamma} - 1 \right), \tag{3}$$

The functional form of ϕ(AV1/AV2) is the same this curve but the constants α and β will change. If we have determined the amplitude and period functions for the sinusoid from the AV1/AV2 ~ 1 range while imposing the constraint $\phi = 0$, then α will be forced to zero. The value of β is modified by the choice of the phase of this zero crossing point.

4. CORRECTION ALGORITHM

The sinusoid function determined above can be used to correct the affected data on an event-by-event basis. The events that are affected must meet the following conditions:

- AMP_SF = 3 (identifies least sensitive amplifier scale)
- $A_1 > A_3$ for the axis - one or both can be affected
- the signals on an even number of taps are above threshold

The last item in this list is the hardest condition to identify. In order to avoid having too many taps trigger above threshold, the value of the threshold used in the comparison is dynamic, changing with the size of the signal from the bottom MCP. Unfortunately, there is no direct measure of the size of the MCP signal in the HRC telemetry; the closest things that we have available are the event pulse height (determined from the total charge collected on the CGCD) and the amplitudes of the tap signals. An additional piece of data is available from the flight instrument:

Table 1. Sinusoid Correction Coefficients

	HRC-I		HRC-S	
Coefficient	V-axis	U-axis	V-axis	U-axis
a	-35.3	20.0	-40.0	-24.0
b	-728.0	-740.0	-655.0	-690.0
c	0.278	0.241	0.279	0.279
d	638.0	979.0	655.0	530.0
β	50.0	12.0	0.0	6.7
γ	0.7	2.0	1.0	1.75
A_1/A_2 threshold	0.14	0.20	0.20	0.20

there are a pair of status bits that indicate whether the event exceeded a commandable event-width threshold, one bit for each axis. This feature was implemented as an aid in identifying events that are likely to have been generated by a charged particle. The event width threshold has been set to 3 so that only for events where the number of taps that are above threshold exceeds 3 on an axis will its corresponding bit be set. The "width-threshold-exceeded" bit is set for only a small fraction of the events when the threshold value is 3. We could lower the event-width threshold to 2 and use the setting of these bits as an aid in identifying the events that require correction but we still need to develop a criterion that will select between events with two or three taps above threshold for use with data taken prior to changing the threshold.

Since we have the freedom to modify the laboratory version of the electronics, we have converted some unused status bits to flag events for which the initial candidate coarse position was incorrect. We hope to use the laboratory data with this modification to determine which relationships among the tap signals and pulse height provide the best chance of discriminating between events with two and with three taps above threshold; however, this work is not yet complete. Even guided by the results from laboratory tests, we must still examine the data from the flight instrument to 1) judge the applicability of the relationships to the flight data and 2) to determine the specific values to be used in any comparisons. As a start and without the benefit of guidance from laboratory data, we have examined the flight data with the goal of find a simple relationship between tap values that will provide the necessary discrimination. A selection that we have found that identifies most of the events that require correction, without including too many that do not, is to choose events for which $A_1/A_2 >$ constant.

Once the affected events are identified, the corrupted tap values can be corrected. Combining the forms of equations 2 and 3 results in an equation for correcting the value of the right side tap:

$$\mathrm{A}_{3\mathrm{corrected}} = \mathrm{A}_{3\mathrm{telemetered}} - \left(\frac{\mathrm{A}_2 + b}{a}\right) \sin\left(2\pi \frac{\mathrm{A}_2 - \beta\left(\left(\frac{\mathrm{A}_2}{\mathrm{A}_1}\right)^{\gamma} - 1\right)}{c\mathrm{A}_2 + d}\right) \tag{4}$$

We determined the coefficients used to correct the data from the HRC-I and HRC-S using calibration observations of the supernova remnant Cas-A. Using a large diffuse target allows us to sample the behavior of the signals on a large number of taps. Only the coarse positions containing X-ray events from the remnant were used, a 10 tap by 10 tap region. The derived coefficients are listed in table 1.

As a test of the correction given by equation 4 and the coefficients in table 1, we applied them to the calibration observation of the bright source 3C273. Figure 8 display the events from the negative side of the V-axis and U-axis taps with the corrections applied to the affected events; in both cases the sinusoidal distortion is greatly diminished. Once the tap data have been corrected, event positions in the detector and their corresponding locations on the sky can be calculated. As mentioned in section 2, the fine position calculated via equation 1 must be modified to account for the information lost due to incomplete charge collection when only three tap signals are used.[13] This degapping correction essentially determines the event location relative to the center of the tap using a polynomial in f_p. Chappell and Murray (1989)[13] showed that a second order polynomial degap correction should be sufficient to correctly position the events to better than one pixel. A fifth-order polynomial has been used in most of the standard processing of HRC data. Such a high order polynomial was adopted in an attempt to correct for the effects of the amplifier ringing. Unfortunately, the fifth-order coefficients were derived from data from the entire width of

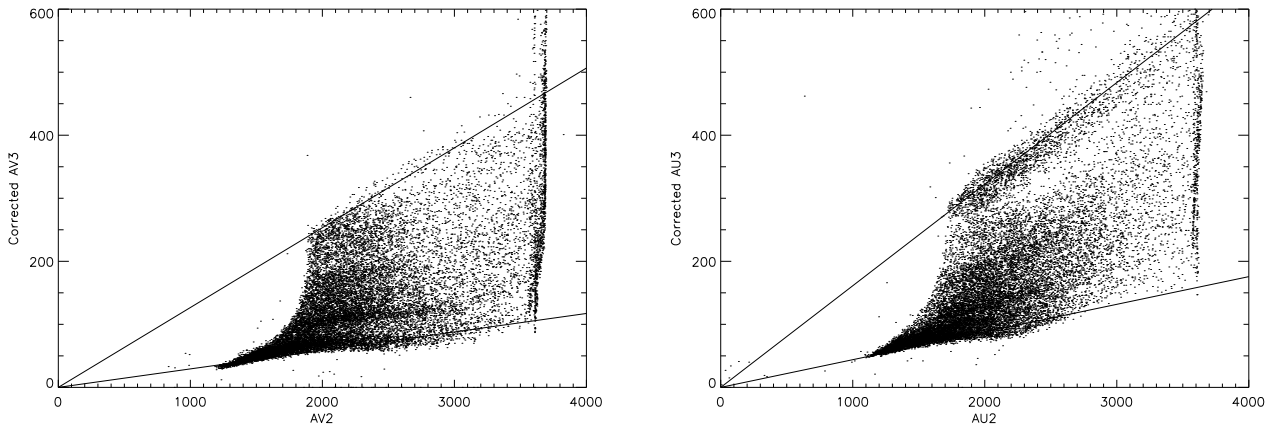

(a) (b)

Figure 8. Right tap versus center tap values after applying corrections: a) V-axis (can be compared to figure 4b). b) U-axis

the detector and as a result do a poor job of correcting for the distortions that are present at any localized area of the detector. Figure 9 shows the encircled energy fraction from the core of 3C273; four curves are presented for cases with and without correcting the tap data for amplifier ringing and using linear or fifth-order degapping corrections. The solid curve and the dot-dashed curve best show the improvement in image quality that results from correcting the tap values; the 50% encircled-energy radius decreases from 4 to 3.2 pixels

5. CONCLUDING REMARKS

The empirically derived algorithm for correcting the data from the CGCD taps that we have presented in this paper reduces the blurring in images introduced by the amplifier ringing. The removal of distortions from the tap signals is not complete and the identification of the effected events is imperfect. One complication that has been ignored in the derivation of the algorithm is that all three tap signals on an axis are affected by the amplifier ringing problem when it occurs. The signature is not as apparent for the two larger signals but since the size of the correction factor is determined from their values some of the residual distortion may be due to distortions within these signals. Similarly, the identification of the affected events can be confused by distortions in these other signals. However, given the demonstrated improvement in image quality, the correction algorithm presented in this paper has been incorporated into the Chadra X-ray Center standard processing software and will be used in re-processing of the data taken since the start of the mission and for the processing of future data.

ACKNOWLEDGMENTS

This work has been supported by NASA contracts NAS8-39073 and NAS8-38248.

REFERENCES

1. Weisskopf, M. C., Tananbaum, H. D., Van Speybrock, L. P., and O'Dell, S. L., "Chandra X-Ray Observatory (CXO): Overview", Proc. SPIE 4012, 2000.
2. Jerius, D., Edgar, R. J., Gaetz, T. J., McNamara, B. R., Schwartz, D. A., Van Speybroeck, L. P., Zhao, P., "Orbital measurement and verification of the Chandra X-ray Observatory's PSF", Proc. SPIE 4012, 2000.
3. Garmire, G. P., Burrows, D., Feigelson, E., Nousek, J., Canizares, C., Clark, G., Collins, S. A., Morrison, J., Pravdo, S. H., Riegler, G. R., "The AXAF CCD imaging spectrometer", Proc. SPIE 597, 261, 1986.
4. Bautz, M. W., Baganoff, F., Isobe, T., Jones, S. E., Kissel, S. E., LaMarr, B., Manning, H. L., Pivovaroff, M., Prigozhin, G. Y., Nousek, J. A., Grant, C. E., Nishikida, K., Scholze, F., Thornagel, R., Ulm, G., "X-ray CCD calibration for the AXAF CCD imaging spectrometer", Proc. SPIE Vol. 3444, 210, 1998.

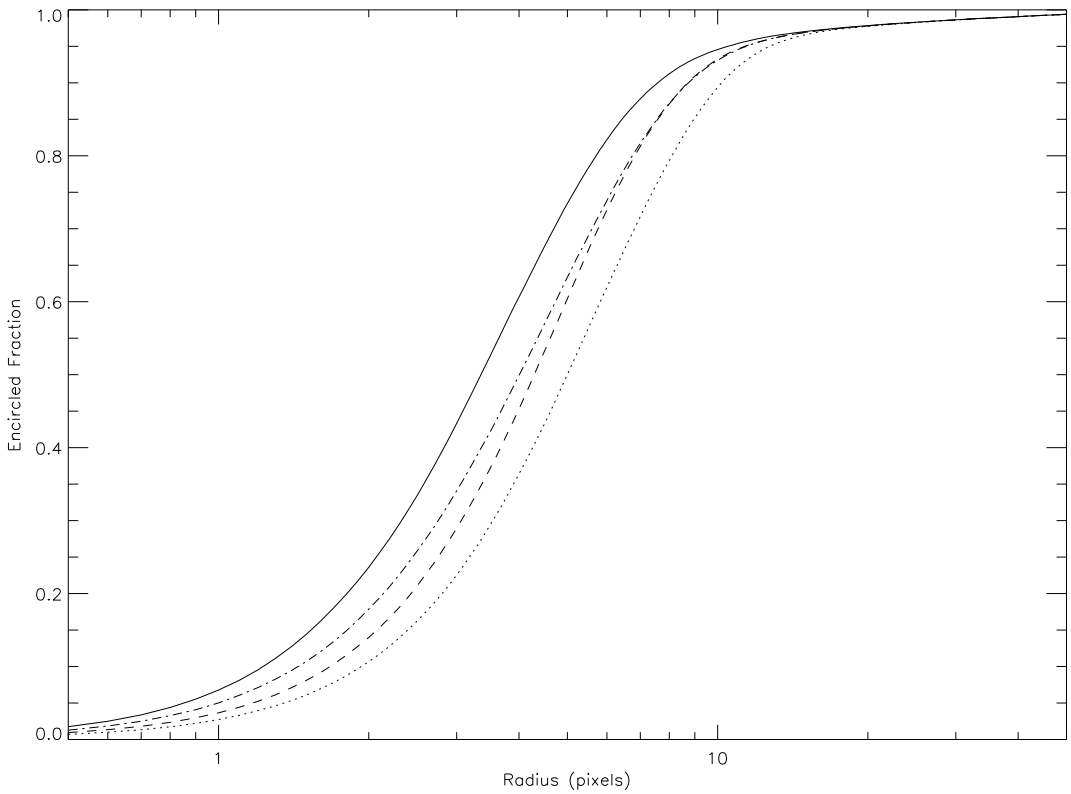

Figure 9. Encircled energy fraction for the core of 3C273 as a function of radius in HRC pixels (1 pixel is ∼0.132 arcseconds). The solid curve is generated from tap data that have been corrected and positions calculated using linear degapping correction. The dashed curve is generated from tap data that have been corrected and positions calculated using fifth-order degapping correction. The dot-dashed curve is generated from tap data that have not been corrected and positions calculated using linear degapping correction. The dotted curve is generated from tap data that have not been corrected and positions calculated using fifth-order degapping correction.

5. Murray, S. S., Austin, G. K., Chappell, J. H., Gomes, J. J., Kenter, A. T., Kraft, R. P., Meehan, G. R., Zombeck, M. V., Fraser, G. W., and Serio, S., "In-flight performance of the Chandra high-resolution camera", Proc. SPIE 4012, 2000.
6. Markert, T. H., Canizares, C. R., Dewey, D., McGuirk, M., Pak, C. S., Schattenburg, M. L., "High-Energy Transmission Grating Spectrometer for the Advanced X-ray Astrophysics Facility (AXAF)", Proc. SPIE 2280, 168, 1994.
7. Brinkman, A. C., Gunsing, T., Kaastra, J. S., van der Meer, R., Mewe, R., Paerels, F. B., van Rooijen, J., Bruninger, H. W., Burwitz, V., Hartner, G. D., Kettenring, G., Predehl, P., Dewey, D., Marshall, H. L., Chappell, J. H., Drake, J. J., Johnson, C. O., Kenter, A. T., Kraft, R. P., Meehan, G. R., Murray, S. S., Ratzlaff, P. W., Wargelin, B. J., Zombeck, M. V., "Description and performance of the low-energy transmission grating spectrometer on board Chandra", Proc. SPIE 4012, 2000.
8. Kenter, A, Chappell, J. H., Kraft, R., Meehan, G., Murray, S. S., Zombeck, M., Hole, K. T., Juda, M., Donnelly, R. H., Patnaude, D., Pease, D., Wilton, C., Zhao, P., Austin, G., Fraser, G., Pearson, J., Lees, J., Brunton, A., Barbera, M., Collura, A., and Serio, S, "In-flight Performance and Calibration of the Chandra High Resolution Camera Imager (HRC-I)", Proc. SPIE 4012, 2000.
9. Kraft, R. P., Chappell, J. H., Kenter, A. T., Meehan, G. R., Murray, S. S., Zombeck, M. V., Donnelly, R. H., Drake, J. J., Johnson, C. O., Juda, M., Patnaude, D. O., Pease, D., Ratzlaff, P. W., Wargelin, B. J., Zhao, P., Austin, G. K., Fraser, G. W., Pearson, J. F., Lees, J. E., Brunton, A. N., Barbera, M., Collura, A., and Serio, S, "In-flight Performance and Calibration of the Chandra High Resolution Camera Spectroscopic Readout (HRC-S)", Proc. SPIE 4012, 2000.
10. Murray, S. S., Chappell, J., Kenter, A., Juda, M., Kraft, R., Zombeck, M., Meehan, G., Austin, G., and Gomes, J., "Event Screening for the Chandra X-Ray Observatory High Resolution Camera (HRC)", Proc. SPIE 4140, 2000.
11. "Chandra Inflight Status Report", `http://asc.harvard.edu/udocs/status.html`
12. Murray, S. S. and J. H. Chappell, "The Advanced X-ray Astrophysics Facility High Resolution Camera", Proc. SPIE, 982, 77, 1988.
13. Chappell, J. H. and S. S. Murray, "Position Modeling for the AXAF High Resolution Camera (HRC)", Proc. SPIE, 1159, 460, 1989.
14. Murray, S. S., Chappell, J. H., Kenter, A. T., Kobayashi, K., Kraft, R. P., Meehan, G. R., Zombeck, M. V., Fraser, G. W., Pearson, J. F., Lees, J. E., Brunton, A. N., Pearce, S. E., Barbera, M., Collura, A. and Serio, S., "AXAF High-Resolution Camera (HRC): calibration and recalibration at XRCF and beyond", Proc. SPIE, 3114, 11, 1997.